Posted: April 24, 2025

A hybrid wind-wave floating platform to ensure a minimum power base load

Abel Arredondo-Galeana[1,*], Gabriel Thomas Scarlett[2], Maurizio Collu[1], and Feargal Brennan[1]

[1]Department of Naval Architecture, Ocean and Marine Engineering, University of Strathclyde; ORCID: 0000-0002-2408-7062
[2]Mocean Energy Ltd;
[*]Corresponding author: abel.arredondo-galeana@strath.ac.uk

Abstract

We develop a novel hybrid wind and wave floating platform for applications that require a minimum power baseload for continuous operation. The hybrid platform consists of three very large pontoons connected with mechanical hinges. The downstream pontoon carries a 5 MW wind turbine on deck. Wave energy is extracted trough hinge motion. By computing numerically a power matrix for wave energy conversion, and assuming mean power production for the wind turbine, we evaluate the performance of the hybrid platform. Performance is gauged by determining periods of time when the hybrid platform meets a minimum wave power threshold, in periods of time of absent wind power. The platform is assessed in three locations with different wind-wave correlation characteristics: One off the coast of Spain, one on the West and one on the East coast of Scotland. Although the platform reduces wind power downtime in the three locations, it is found that it has better performance in locations with high wave power density and low to intermediate wind-wave correlation indices. The hybrid platform proposed in this work is enticing for offshore applications that run in steady state. For example, hydrogen electrolysers, which require a minimum power supply for lasting operation.

1 Introduction

Floating offshore wind turbines are expanding to deep water (>100 m) with ever increasing large wind turbines. Nonetheless, deep water operations pose significant cost related challenges for offshore renewable (ORE) technology (43). For floating wind, the "modus operandi" consists of one very large wind turbine per floating foundation (1; 30). This poses significant engineering and cost challenges to design reliable floating structures that can carry massive wind turbines and can provide platform stability (2; 33). In addition to structural and cost related challenges, larger transmission distances combined with the intermittency of wind, produce an increase in dispatch costs, and can also incur into associated energy storage costs to satisfy peak demand.

A possible solution to reduce the costs of floating offshore wind, relies in the design of hybrid offshore renewables. Hybrid offshore renewables have the capacity to reduce the levelised cost of energy of offshore wind farms, through reduction of dispatch costs and peak generation requirements (12; 18; 20; 31; 44). In particular, wind and wave collocation and hybrid platforms have the potential to share installation facilities and thus, reduction of dispatch costs (31). Secondly, wave energy has a higher predictability and mean power density per meter than other offshore renewable alternatives, such as solar energy (32; 34). Thirdly, wave energy extraction has also the capability of suppressing loads in neighboring wind turbine structures, through passive or active control (9; 17). Hence, hybrid wind and wave floating platforms have emerged as possible candidates to reduce floating ORE costs in recent years.

Further to cost reductions, hybrid wind and wave platforms can be designed to provide a continuous minimum power baseline for offshore applications. We consider the case of hydrogen proton exchange membrane (PEM) electrolysers, whose operational life is reduced when the power baseload drops below 20% of their rated capacity (27). Hence, in this work, we investigate to what extent wave power can ensure a minimum power baseload and reduce wind downtime power.

We propose a novel hybrid platform to supply a continuous power baseload. The design of the platform consists of a three pontoon barge type floating structure connected with two hinges. Hinge motion is used to extract wave energy. While a 5 MW wind turbine is installed in the downstream pontoon. Barge floating structures have been considered in earlier works as foundations of wind turbines (22; 19), while hinge motion has been studied and implemented successfully for wave energy conversion (26; 28; 29; 48; 47; 36). Nonetheless, the combination of barges and hinges into a hybrid platform design to provide a minimum baseload has not been considered in the literature. Note that hybrid platforms that combine wind and wave energy conversion have exist in the literature, but are mostly inspired on semi-sub floating structures (16; 37; 38). Hence, the concept proposed in this work is based on an alternative design based on a hinged connected very large floating structures (VLFS).

We assess the hybrid platform in three different locations with different wind-wave resource correlation. One off the coast of Spain, with a low correlation index, and two off the coast of Scotland, with higher correlation indices. We hypothesise that the platform performs better in the low correlation site. Note that typically, in wind and wave correlation studies, only metocean data is considered (6; 23; 15). However, as part of the novelty of this work, a numerical model is used to estimate the power matrix of the platform subject to a range of sea states. Because the wind turbine is mounted downstream of the platform, a reduced range of pitching motions is considered and the mean power curve of a 5 MW wind turbine is utilised to compute the wind turbine power. The performance of the hybrid platform to provide a minimum baseload, and to reduce wind power downtime is assessed. Additionally, the role of wind and wave power density, and correlation index are analysed.

The structure of the paper is laid out as follows. First, the hybrid platform is introduced. Then, the three proposed locations for the hybrid concept are presented. One with a low wind and wave correlation index off the coast of Spain, and two with higher correlation indices, off the west and east coast of Scotland. Subsequently, the numerical model used to asses the dynamics of the platform subject to irregular waves is presented. The influence of the wind turbine on platform motion is assessed and the power matrix of the platform is quantified. The performance of the hybrid platform is discussed in terms of downtime power reduction for the three proposed locations, for a period of 20 years of metocean data. Lastly, the conclusions of the work are presented.

2 The hybrid platform

In this Section, we introduce the hybrid platform. The platform comprises three pontoons and two hinges, as depicted in Figure 1. The platform is designed to carry the NREL 5 MW wind turbine. The particulars of the wind turbine are shown in Table 1. Figure 1 shows that the turbine is supported by the downstream pontoon at the stern of the platform, and wave energy is extracted at the hinge locations. The wind turbine actively yaws into the main wind direction. While the platform passively yaws into the main wave direction, through a single point mooring line (7). The connection point of the mooring line is positioned at the bow of the platform. The single point mooring line, and passive yaw mechanism of the platform, ensures that the rotational axis of the hinges is oriented parallel to the crest of the waves to maximise hinge motion. The 5 MW wind turbine is selected to feed a PEM electrolyser rated at 5 MW. The PEM electrolyser is located in a different floating platform and is not depicted in the diagram of Figure 1.

By adjusting the draft of the pontoons shown in Figure 1, and assuming a fixed pontoon surface area, the required buoyancy for the wind turbine and the pontoon can be achieved. Considering water density $\rho_g =$ 1025 kg/m^3, and a very large floating structure (VLFS) pontoon surface area of $58\,\mathrm{m}\,\times\,58\,\mathrm{m}$, a draft of $1.0\,\mathrm{m}$ per pontoon is sufficient to provide a buoyancy force $\mathrm{B} \approx 5 \times \mathrm{W}_t$, where W_t is the weight of the turbine. The water displacement of each pontoon is 3,364 m^3.

The ability of the hybrid platform to resist rolling motion is determined through the width of the platform. Following (49), where the rotor plane of the turbine is parallel to the direction of the wave, we compare the moment due to the mean thrust of the turbine and the restoring moment. Considering that for a NREL 5 MW turbine, $D = 126$ m, a width of $w \approx 0.5D$ limits the rolling angle of the platform to $\phi < 0.5°$. Note

Wind turbine	Hub height (m)	Rotor width	Rated speed	Cut in speed	Cut out speed	Mass	Rated power
NREL turbine	90 m	126 m	11 m/s	3 m/s	25 m/s	697 tonnes	5 MW

Table 1: Wind turbine particulars for the 5MW NREL concept (21).

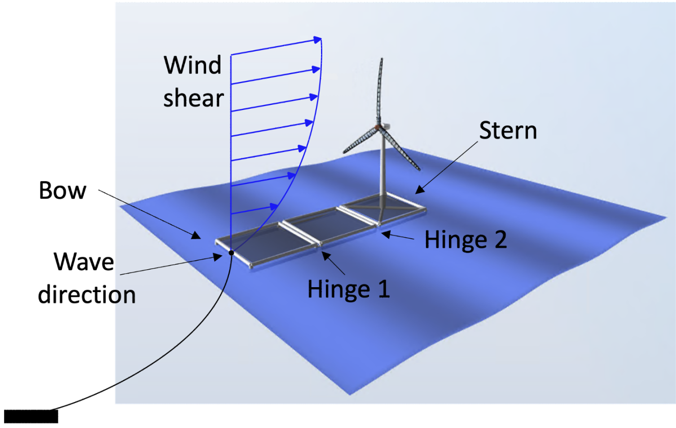

Figure 1: Three pontoon hybrid platform with turbine mounted downstream of the platform. Wave energy is harnessed through hinge motion. The single point mooring line upstream of the platform allows for passive yaw into the main wave direction.

that the selection of a small scale wind turbine ($\leq 5\,\mathrm{MW}$), facilitates the structural design and allows for ease of transportation and assembly (2).

3 Site selection

Site selection is an important consideration in the performance of a hybrid wind-wave floating platform. Low wind-wave correlation sites could be beneficial to exploit the complementarity of wind and wave power. However, whether this holds true, or whether the performance of the platform subject to intermediate and high correlation sites changes, remain open questions. Hence we consider the three locations depicted in Figure 2. A swell dominated, low correlation site, off the North West coast of Spain, Villano Sisargas (VS), and higher correlation sites, one off the West coast of Scotland, NE3, which is still swell dominated, and one in the North Sea and off the East coast of Scotland, NE8, which is expected to have a higher wind wave correlation due to a shorter fetch. The selection of the sites is restricted to three locations with different wind and wave correlation characteristics, low, intermediate and high correlations, but the methodology to assess the performance of the hybrid platform is applicable to further locations.

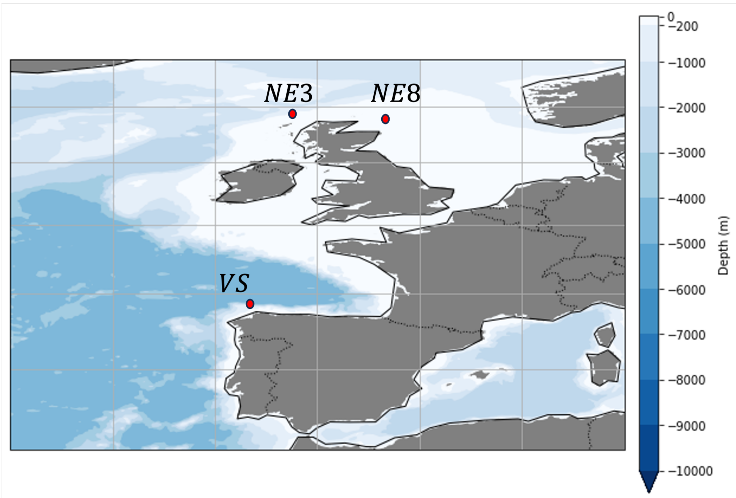

Figure 2: Selected sites for analysis of hybrid wind wave platform: Villano Sisargas (VS) off the coast of Spain, NE3 and NE8, off the west and east coast of Scotland.

The ESOX tool (LAUTEX ESOX.), which uses the ERA5 data base, is used to sample the metocean data of the selected locations. The temporal resolution of the ERA5 data base is hourly, while the spatial resolution is $0.25° \times 0.25°$. In Table 3, the geographical coordinates and the average metocean properties of the

Location name	Country	Coordinates	α	U_{10}	U_{100}	U_{hub}	H_s	T_p
NE8	Scotland	N 58.25°, W 1.5°	0.0884	8.36	10.25	10.05	1.8425	8.0486
NE3	Scotland	N 58.75°, W 6.5°	0.1766	8.64	10.46	10.27	2.6023	10.6302
Villano Sisargas	Spain	N 43.5°, W 9.21°	0.1787	7.73	9.38	9.20	2.4997	10.7493

Table 2: Average wind and wave metocean conditions for NE8, NE3 and Villano Sisargas for years 2000-2019 from ESOX database (LAUTEX ESOX.).

locations depicted in Figure 2 are provided. The metocean properties listed in Table 3 are mainly wind speed at hub height (U_{hub}), significant wave height (H_s) and mean peak period (T_p). To compute U_{hub}, a mean wind speed power law coefficient (α) is computed by considering the mean wind speed at 10 m (U_{10}) and at 100 m (U_{100}). Twenty years of metocean data, ranging years 2000-2019, are considered to compute the metrics shown in Table 3.

The correlation coefficient can be used as an index of suitable locations for hybrid floating platforms (6; 23; 15), and is defined through the Pearson's correlation such that

$$C(x, y, \tau) = \frac{1}{N} \sum_{i=1}^{N-\tau} \left[\frac{(x_i - \overline{\mu}_x) \cdot (y_{i+\tau} - \overline{\mu}_y)}{\sigma_x \sigma_y} \right], \quad (1)$$

where x and y are the correlation variables, i is the instant in time, τ is the time lag between x and y. In this case we consider $\tau = 0$. Then, $\overline{\mu}_x$ and $\overline{\mu}_y$ are the mean of the correlation variables, respectively, σ_x and σ_y are the standard deviation of x and y, respectively, N is the total number of instances in the time series. In this work, the correlation variables used in Equation (1) are the wave power density (in deep water) per meter wave crest ($\mathrm{W/m}$), defined as

$$\rho_{wave} = \frac{\rho_s g^2 H_s^2 T_e}{64\pi}, \quad (2)$$

and the wind power density per swept area ($\mathrm{W/m^2}$), defined as

$$\rho_{wind} = \frac{\rho_a U_{hub}^3}{2}. \quad (3)$$

In Equations (2) and (3), ρ_s is the water density, g is the gravity of Earth, H_s is the significant wave height, T_e is the wave energy period, ρ_a is the density of air and U_{hub} is the wind speed at hub height.

To compute the wave energy power (P_{wave}) provided by the hybrid platform, a power matrix considering the effect of irregular waves is developed. Hence, H_S and T_P are used as inputs to the matrix. In the next section, we introduce the hydrodynamic model used to compute the power matrix of the WEC. The power of the turbine (P_{wind}) is assessed through the power curve of the NREL 5MW wind turbine under the assumption that minimal pitching and heave motions do not alter the mean power performance of the turbine (45). The assumption of reduced amplitude motions is further assessed in the results section of this manuscript.

4 Numerical model

The numerical model utilised in this work is the frequency domain approach developed for hydroelastic VLFS in Zhang et al. (48) and applied for hinged connected dual raft in Zhang et al. (48). The method was applied by Arredondo-Galeana et al. (3) to validate experimental measurements of a rigid and hinged connected VLFS platform. In this work, the numerical model is adapted to include wind turbine loading and the effect of the wave power take off in a three pontoon dual hinge floating system. The main assumptions of the model are summarised as follows.

Consider Figure 3, showing three pontoons connected by two mechanical hinges. The mechanical hinges are denoted with red circles. Each pontoon is discretised into a finite number of segments n and the total number of segments of the platform is $N = 3 \times n$. Each segment is represented by a black circle in Figure 3. The black circles are lump masses with 6 degrees of freedom each, such that $x_i = [x, y, z, \phi, \theta, \psi]$, where x, y, z, ϕ, θ and ϕ refer to surge, sway, heave, roll, pitch and yaw, respectively. Then, the motion vector of the platform is **X** $= [x_1 ... x_N]'$. The lump masses are connected to each other with elastic beams with structural stiffness $\mathbf{k}$ to account for any hydroelastic deformation in the platform. The connection between mechanical hinge and adjacent lump mass is not an elastic beam, instead, it is a rigid connection. The rigid connections are highlighted in Figure 3. They transfer the motion of the adjacent lump mass to the mechanical hinge through rigid body assumptions. A stiffness matrix $\mathbf{K}_S$ of $N \times N$ elements for the platform is constructed by concatenating the stiffness of the individual beam elements $\mathbf{k}$.

The balance of forces and the influence of the two hinges in the motion response of the platform is given by:

$$\begin{bmatrix} -\omega^2(\mathbf{M}+\mathbf{A}(\omega)) - i\omega(\mathbf{B}(\omega)+\mathbf{D}_{\mathrm{PTO}}) + \mathbf{C} + \mathbf{K}_S & \Xi_1^T & \Xi_2^T \\ \Xi_1 & \mathbf{0} & \mathbf{0} \\ \Xi_2 & \mathbf{0} & \mathbf{0} \end{bmatrix} \begin{bmatrix} \mathbf{X} \\ \mathbf{F}_1 \\ \mathbf{F}_2 \end{bmatrix} = \begin{bmatrix} \mathbf{F}_{wave} + \mathbf{F}_{wind} \\ \mathbf{0} \\ \mathbf{0} \end{bmatrix}, \quad (4)$$

where the first line of the system of Equations (4) shows the balance of external forces applied to the hybrid platform, where $\mathbf{M}$ is the mass, $\mathbf{A}(\omega)$ is the added mass, $\mathbf{B}(\omega)$ is the radiation damping, $\mathbf{D}_{\mathrm{PTO}}$ is the power take off damping (D_{PTO}), which constitutes a force that is proportional to the velocity $i\omega\mathbf{X}$ (14), $\mathbf{C}$ is the restoring matrix, K_S is the structural stiffness matrix to account for elastic effects of the platform (3; 46), $\mathbf{\Xi_1^T} F_1$ and $\mathbf{\Xi_2^T} F_2$, are the forces at the two hinges translated to the adjacent lump masses of the hinge, F_{wave} is the wave excitation force and $\mathbf{F}_{wind}$ is the wind loading in the frequency domain. Viscous losses are neglected as potential flow models have shown to be accurate to predict the motion response of hinged connected structures, where the pontoon length is significantly greater than the draft (3). Additionally, for low mooring line stiffness, numerical models that include a consideration for mooring line forces yield similar results to models that do not consider them (11). Hence, in this work mooring line forces are not considered, since the mooring line needs to allow pitch and heave motion of the platform.

The second and third equations $\mathbf{\Xi_1 X} = 0$ and $\mathbf{\Xi_2 X} = 0$, shown in Equation (4), respectively, arise because the spatial location of the hinges, is the same, when determined either from the left or the right adjacent lump mass. Consider, for example hinge 1, with points a and b located to the left and right of the hinge. Then because the two points are located at the hinge, the position vectors of points a and b yield

$$x_a - x_b = 0. \quad (5)$$

Assuming the rigid body connections shown in Figure 3, x_a and x_b can be computed by projecting the motion of the adjacent lump masses to the left and right of the hinge to points a and b, respectively, such that

$$x_a = \mathbf{L}_a x_A \qquad \text{and} \qquad x_b = \mathbf{L}_b x_B, \quad (6)$$

where A and B are the lump masses adjacent to the left and right of the hinge, $\mathbf{L}_a$ and $\mathbf{L}_b$ are the Lagrangian motion transformation matrices between lump masses A and B, to points a and b, respectively. Note that $\mathbf{L}_a$ and $\mathbf{L}_b$ are matrices of 5×6 because the 6 degrees of freedom of the adjacent lump mass only affects 5 degrees of freedom of the hinge, since the hinge is free to pitch around its own axis

Lastly, x_A, and x_B are the position vectors of A and B, respectively, with 6 degrees of freedom. Then, by substituting Equation (6) into Equation (5), adding the influence of the non adjacent lump masses to the motion of the hinges, and considering that x_A and x_B are part of motion vector $\mathbf{X}$, we can write

$$[0_1 \;\; \mathbf{L}_a \;\; -\mathbf{L}_b \;\; 0_2]\mathbf{X} = 0, \quad (7)$$

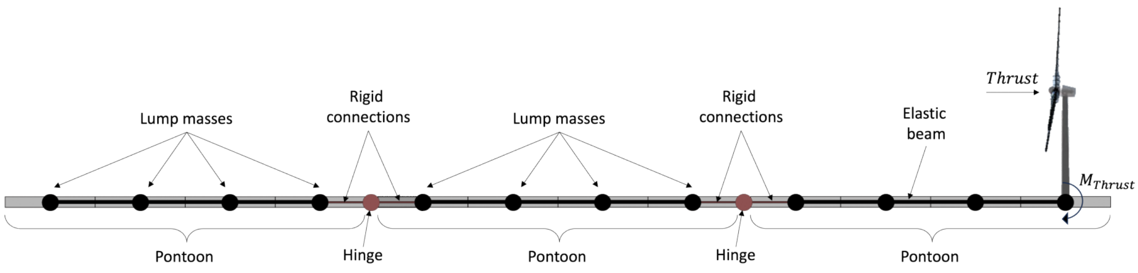

Figure 3: Discrete beam element model for hinged VLFS with mass and turbine thrust incorporated.

where $\mathbf{0_1}$ and $\mathbf{0_2}$ are zero matrices of dimensions $5 \times 6 \times N_l - 1$ and $5 \times 6 \times N_r - 1$, respectively, where, N_l and N_r are the total number of lump masses to the left and right of the hinge, respectively. Then,

$$\mathbf{\Xi} = [0_1 \quad \mathbf{L}_a \quad -\mathbf{L}_b \quad 0_2], \tag{8}$$

is the motion constraint matrix.

The hydrodynamic loads acting on the platform and stated in the first line of Equation (4) are solved through a multi-body approach (2), where the loads are solved for each segment or body of the platform separately. Then, the effect of the hinges or rigid connections is considered through the full system of equations shown in Equation (4). Therefore, in an initial step, the platform is segmented into N number of bodies that are meshed in a potential flow numerical solver. A small gap is left between each body. The hydrodynamic forces in the form of added mass $\mathbf{A}(\omega)$, radiation damping $\mathbf{B}(\omega)$ and Froude-Krylov forces ($\mathbf{F}_{wave}$) are computed for each body and for the influence of each body in the neighboring bodies. The shape of the matrices is $N \times N$ for $\mathbf{A}(\omega)$ and $\mathbf{B}(\omega)$, and $N \times 1$ for the $\mathbf{F}_{wave}$ vector. For the case of this work, the hydrodynamic matrices were computed in Hydrostar software (2; Bureau Veritas). Lastly, note that each body or segment of the platform has a corresponding mass **M** and hydrostatic **C** matrix. For details on the shape of $\mathbf{K}_S$, **C** and **M**, see for example (48).

Wind turbine loads in the hybrid platform are accounted for by incorporating the mass and the inertia of the monopile and rotor-nacelle-assemble (RNA), to the lump mass where the wind turbine is mounted. We describe the modifications to matrix **M** to account for the mass and inertia of the wind turbine in Appendix A. Furthermore, the mean wind turbine thrust is applied as a constant moment at the base of the platform where the wind turbine is installed. The external wind turbine load is denoted as F_{wind} in Equation (4). A constant moment is considered for wind turbine loading under the assumption that the mean loads do not change when the pitching motions of the turbine are maintained below 10° (45). This assumption is verified in the Results section of the manuscript.

In this paper, we are interested in the motion response of the platform, that is, in the $\mathbf{X}$ vector of Equation (4). Specifically in the pitch response θ. The relative pitch of the hinge, hereafter referred to as flex of the hinge ($\Delta\theta$) is defined as

$$\Delta\theta = \theta_1 - \theta_2, \tag{9}$$

where θ_1 and θ_2 are the pitch angles computed for the left and right adjacent lump masses to the hinge. The mean power captured by the hinge, in the frequency domain is defined as

$$\overline{P} = \frac{1}{2}\omega^2 d_{\mathrm{PTO}} |\Delta\theta|^2, \tag{10}$$

where ω is angular frequency of the hinge, d_{PTO} is the damping coefficient, where following (48), is applied to the pitching motion degree of freedom of the adjacent lump masses to the hinge, and where $\Delta\theta$ is the flex angle of the hinge in radians per meter wave height. Later in the manuscript, we compute numerically the optimum value of d_{PTO} to maximise wave energy extraction.

To consider the influence of irregular waves, a wave amplitude spectrum, $S(\omega)$, is discretised in the frequency domain and used to generate individual waves of wave amplitude A_j, where j, in this case, is the index denoting the individual wave. The amplitude of the discrete wave components is given by

$$A_j = \sqrt{2S(\omega_j)\Delta\omega}, \tag{11}$$

where $S(\omega_j)$ is the amplitude of the spectrum at the j-th frequency ω_j, and $\Delta\omega$ is the discretisation step of the spectrum. Similar to the irregular wave analysis carried out in Arredondo-Galeana et al. (4) for a wave energy converter, we utilise the definition of the JONSWAP spectrum provided by the DNV Environmental Conditions And Environmental Loads Practice Manual (13). Then, the average power for a given sea state is computed as

$$P = \sum_{j}^{N} \overline{P}_j A_j^2, \tag{12}$$

where j indicates the j-th frequency and N is the total number of frequencies in which the JONSWAP spectrum is discretised, $\overline{P}_j$ is the average power of the j-th frequency computed with Equation (10) and A_j is the j-th wave amplitude computed with Equation (11).

5 Results

Turbine influence in platform motion

In this Section, we assess the influence of the turbine in the heave (Δz) and flex response ($\Delta\theta$) of the mechanical hinges of the platform. Because of the rigid body assumption, both Δz and $\Delta\theta$ are important parameters that influence the motion at the hinge location, and therefore have an impact on wave energy conversion. Furthermore, by computing $\Delta\theta$, using Equation (9), we can understand the range of pitch motion of the platform in the vicinity of the hinge. The range of pitch motion can indicate whether the power performance of the turbine could remain constant, as demonstrated in the literature (42; 43).

As an initial step of analysis into the dynamics of the platform, we consider first the response of the VLFS only, without wind turbine loading, and assuming an underdamped response (25), i.e. unloaded hinge. The response amplitude operator (RAO) curves for heave (Δz) and flex ($\Delta\theta$) of the upstream and downstream hinges are plotted in $\mathrm{Figure\,4a}$ and Figure 4b, respectively. Both Δz and $\Delta\theta$ are normalised by wave amplitude and plotted as a function of the wave period. In both Figure 4a and Figure 4b, the Δz and $\Delta\theta$ of the "VLFS only" case are plotted with blue solid lines for the upstream hinge, and with black solid lines for the downstream hinge. Subsequently, the Δz and $\Delta\theta$ of the VLFS with the wind turbine are considered. The VLFS and wind turbine heave and flex RAO results are plotted with scattered markers in both Figure 4a and Figure 4b, respectively. The color notation is consistent with the VLFS only case, and blue markers are used for the upstream hinge, and black markers are used for the downstream hinge in both of the figures. Because we consider an underdamped response, the computed downstream hinge RAOs are compared with experimental Δz and $\Delta\theta$ measured at the Kelvin Hydrodynamics laboratory at the University of Strathclyde (2). The experimental data is plotted with red scattered markers in both 4a and Figure 4b. Note that in (2), the VLFS is hinged connected with three pontoons and without a turbine, and only Δz measurements are available at locations that correspond to the lump masses shown in Figure 3. Therefore, in Figure 4a, a factor of $L\theta$ is added to the heave response of the lump mass next to the hinge, to account for L, which is the distance from the adjacent lump mass to the hinge and for θ, which is the numerically computed pitch angle of the lump mass next to the hinge. The experimental error in Δz was estimated to be approximately 5% in (3) and is depicted with the error bars in Figure 4a.

Then in Figure 4b, the experimental flex is computed by deriving the pitch angle of each pontoon, from heave measurements of different points located along each pontoon. The layout of the heave measurement points on the hinged connected VLFS is available in (2). To reduce the error in the pitch angle estimation, the maximum Δz of the two most distant points in a pontoon were utilised. Subsequently, the flex angle $\Delta\theta$ was computed. The error was estimated through error propagation analysis (40), considering the heave error as the input, from the heave measurement and error bars are plotted in Figure 4b. Lastly, adjacent averaging was applied to the experimental data in both Figure 4a and Figure 4b to improve smoothness.

Figure 4a shows that when $T > 10\,\mathrm{s}$, the heave response of the upstream and downstream hinge has a similar behavior. As T grows, i.e. $T \geq 20\,\mathrm{s}$, $\Delta z \approx 1$. This asymptotic condition is characteristic, when the wave wavelength is significancy longer than the length of the full platform (3). In contrast, when $T \leq 10\,\mathrm{s}$, the heave response of the upper hinge is higher than the response of the downstream hinge. This is because, at higher frequencies, i.e. shorter wavelengths, the upstream hinge absorbs most of the energy, attenuating the wave downstream. Figure 4a shows that in terms of heave response, the influence of the turbine is almost negligible, and therefore, most of the heave dynamics of the platform are governed by hydrodynamic loading.

Regarding hinge flex motion, Figure 4b shows that the upstream and downstream hinge have a similar behavior also when $T > 10$ s. In contrast, for shorter waves, i.e. $T \leq 10$ s, the upstream hinge has a more pronounced response. Furthermore, Figure 4b shows that the flex resonant frequency of the upstream hinge occurs at about $T \approx 8.5$ s, whilst for the downstream hinge the resonant peak occurs at $T \approx 9.5$ s. At the resonant peaks, the highest flex angle at the upstream hinge is approximately 5$^\circ/\mathrm{m}$. In contrast, the highest flex angle of the downstream hinge is approximately 4.5 $^\circ/\mathrm{m}$. Noteworthy, the influence of the wind turbine, denoted by the circular markers in Figure 4b, show a negligible effect also in the flex angle of the platform, with a slight increase in the upstream hinge maximum flex peak which grows from 5$^\circ/\mathrm{m}$ to approximately 5.2$^\circ/\mathrm{m}$.

Two critical performance factors stand out from Figure 4b. Firstly, it can be seen that the peak flex response of the upstream and downstream hinges lie over the range of $8\,\mathrm{s} \leq T \leq 10\,\mathrm{s}$. This range of periods typically coincides with peak periods of high probability sea states in the European Atlantic Coast (5; 4). Secondly, because the upstream hinge absorbs more wave energy and imposes higher flex angles than the downstream hinge, then the optimum position of the wind turbine, in terms of motion disturbance is the downstream pontoon. Furthermore, we recall that the results presented here are for an underdamped response. Additional control strategies, such as overdamped and optimal PTO damping (35), can be implemented to maximise power extraction in the upstream hinge, and mitigating further the motion of the downstream hinge.

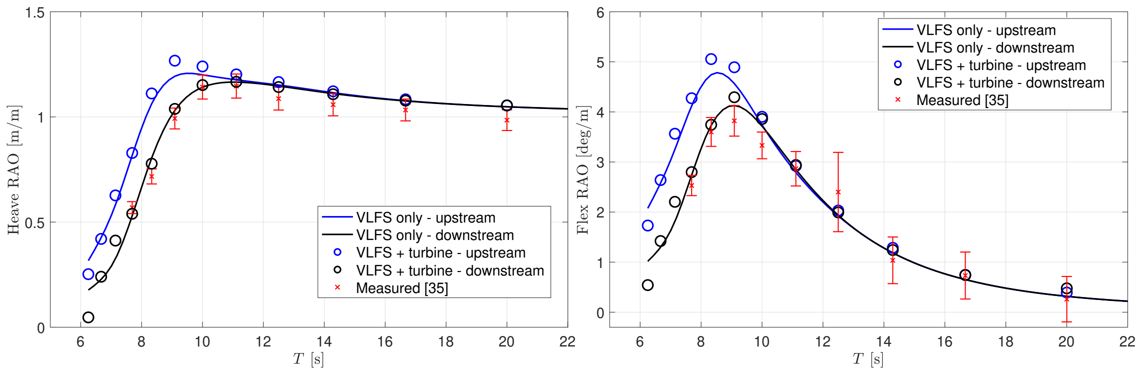

Figure 4: a) Heave (Δz) and b) flex ($\Delta \theta$) RAO curves for hinged VLFS only and hinged VLFS with wind turbine. Results are computed by considering an underdamped response and comparing VLFS only curve to RAO data measured in downstream pontoon (2).

With respect to wind turbine power performance, it has been demonstrated that for a low range of pitch amplitude motions, the mean power performance of the turbine remains relatively stable (42; 45). Hence, because in general, the pitch angle of the downstream pontoon is the lowest, and remains typically below or circa to 10°, then the range of motion shown in Figure 4b confirms that a constant power performance for the wind turbine can be considered. In particular, the turbine is also equipped with power control capabilities to provide a stable power output above rated speed (45). Therefore, we consider the mean curve power of the NREL 5 MW turbine to compute the power production of the turbine.

WEC performance

We perform a sweep of different d_{PTO} values at three different wave frequencies (0.3 Hz, 0.5 Hz and 1.0 Hz) to find out the optimum d_{PTO} value for wave power production. Figure 5a shows the normalised total flex angle of the platform and the normalised mean power computed with Equation (10) versus d_{PTO}. For clarity of the figure, only the case of 0.5 Hz is presented in 5a, although the rest of the cases (0.3 Hz and 1.0 Hz) show similar performance. It can be seen in Figure 5a, that as $d_{\mathrm{PTO}} \geq 1\,\mathrm{GNms/rad}$, the total flex starts to decrease. In contrast, the normalised power starts to increase reaching its maximum level at $d_{\mathrm{PTO}} = 5.5\,\mathrm{GNms/rad}$, while the total flex drops to about 62% of the underdamped response. Hence, for the remaining of our study, the optimum d_{PTO} is selected as operating point of the hybrid platform.

The power matrix of the hybrid platform is computed for a total of 30 sea states. The sea states corresponded to the combination of significant peak periods (T_p) and significant wave heights (H_s) over the range of 6 s to 16 s in increments of 2 s, and over the range of 1 m to 5 m in increments of 1 m, respectively. The power per sea state is computed with Equation (12) and results are interpolated to a finer grid of 50 $\times$ 50 elements. The matrix is computed assuming optimal damping and average turbine loading on the platform. Results are presented in Figure 5.

The power matrix shown in Figure 5 highlights that the wave energy subsystem of the hybrid platform has a broad band response with the highest values extending over the range of 10 s to 14 s, with a local maximum at $H_s = 5\,\mathrm{m}$ and at $T_p = 12\,\mathrm{s}$. The broad band response shown in the power matrix is associated to the combined effect of the two hinges. Additionally, damping flattens the RAO curve and shifts the peak response to the right hand side of the peaks detected in Figure 4b, which were located between $8.5, \mathrm{s} < T < 9.5\,\mathrm{s}$. Lastly, larger T_p sea states contain more energy (see Equation (12)). This also contributes to the maximum response of the power matrix shown in Figure 5 to be detected at $T_p = 12\,\mathrm{s}$, and to the right hand side of the peaks identified in Figure 4b. Note that the shape of the power matrix coincides with related studies on wave energy generation through floating platforms composed by hinged

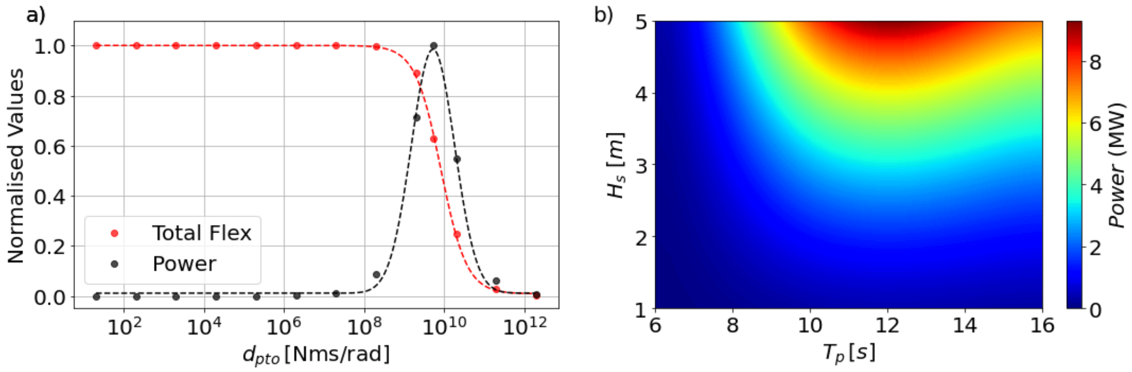

Figure 5: a) Normalised total flex and power versus different values of power take-off damping (d_{PTO}) and b) wave power matrix of hybrid platform. Considering $d_{\mathrm{PTO}} = 5.5\,\mathrm{GNms/rad}$.

elastic plates (39).

We recall that the purpose of this paper is to assess the performance of the hybrid platform in sites with different metocean properties, i.e. swell dominated sites versus wind-wave dominated sites (see Figure 2). Therefore in the next section, we characterise NE3, NE8 and VS, in terms of wave and wind power densities (Equations (2) and (3)) and in terms of wind and wave correlation index (Equation (1)). Subsequently, we utilise the power matrix computed in Figure 5, and the power curve of the NREL 5 MW wind turbine to assess the performance of the hybrid platform to provide a minimum power threshold and reduce wind power downtime. Note that the power curve of the NREL 5 MW wind turbine was computed in software ASHES (41).

Power density correlation of sites

An important aspect that will affect the performance of the hybrid platform is the availability of wind and wave power. Hence, the monthly wind and power density averaged over 20 years (2000-2019) are shown in Figure 6a and Figure 6b, respectively. Results are shown for the three selected sites, VS, NE3 and NE8 with red, blue and black marker lines, respectively. Note that the monthly wind and power densities are computed by averaging the hourly data of U_{hub}, H_s and T_p and by using Equation (3) and Equation (2), respectively

It can be seen that both Figure 6a and Figure 6b show a bathtub shape where the highest power density is available in the winter months from November to February, and the lowest power density is available in the summer months from May to August. Noteworthy, the wind power density is similar for the three locations in Figure 6a, with a slight drop towards the edges in VS. In contrast, Figure 6b shows that the wave power density is lowest in N8 throughout the full year, as opposed to the wave power density of open sea locations such as N3 and VS. This could be a determining factor in the performance of the hybrid platform.

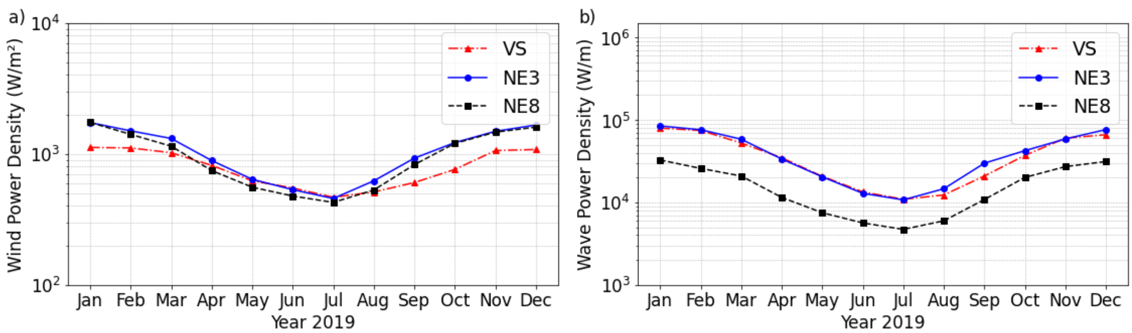

Figure 6: Monthly average a) wind and b) wave power densities for VS, NE3 and NE8 averaged over 20 years from 2000 to 2019.

Prior to analysing the performance of the hybrid platform, and as a subsequent step in site characterisation, we now look at the correlation between wind and wave in NE3, NE8 and VS. The monthly average wind and wave power correlation coefficients are presented in Figure 7, where the vertical axis shows VS, NE3 and NE8 from top to bottom, and the horizontal axis shows the monthly coefficients averaged over 20 years (2000-2019). Hourly data and Equations (2), (3) and (1) are used to compute the monthly average correlation coefficients. The colorbar of Figure 7 shows the color code for the correlation coefficient, where a high value corresponds to dark blue ($C > 0.7$), and a low correlation value corresponds to light yellow ($C < 0.4$).

Figure 7 confirms that throughout the year, VS off the coast of Spain has the lowest correlation coefficients, with a yearly average value of 0.35, compared to 0.63 and 0.75 for NE3 and NE8, respectively. The locations selected off the coast of Scotland have clearly higher correlation coefficients than those in VS. NE8, in the North Sea, has higher correlation coefficients than NE3, possibly because NE3 is exposed to the Atlantic Ocean (see Figure 2), where swell waves might still be present, as in the case of VS. In contrast, N8 is located in the North Sea and surrounded by continental masses. Therefore, sea states do not fully develop as in the open ocean, and waves are directly related to local wind.

In the following Section, we investigate whether the performance of the hybrid platform is superior in low correlation sites, such as VS, or whether the availability of power is more important to the performance of the hybrid platform.

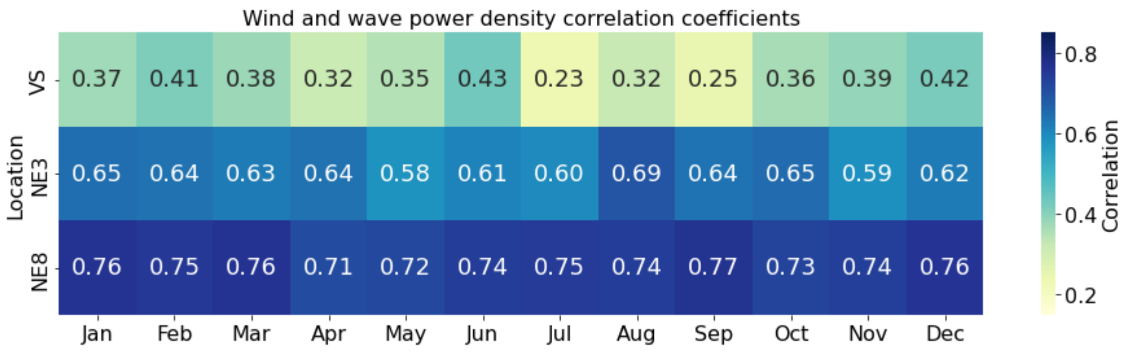

Figure 7: Monthly average wind and wave power density correlation coefficients, averaged over 20 years (2000-2019), for VS, NE3 and NE8.

Hybrid platform assessment

We investigate the performance of the hybrid platform in the three different locations depicted in Figure 2. The locations are: Villano-Sisargas (VS) off the coast of Spain, NE3 off the west, and NE8 off the east coasts of Scotland. We recall that VS, NE3 and NE8 have low, intermediate and high wind wave correlation indices, respectively, as indicated in Figure 7.

As performance metric, the power downtime of wind turbine versus hybrid platform is compared. Power downtime in the hybrid platform is considered when the power drops below a certain power threshold. For the case of the hybrid platform, we consider 1 MW (20% rated power of 1 PEM electrolyser rated at 5 MW - the same rating as the wind turbine), as the power production threshold. In contrast, for the case when only the wind turbine operates, power downtime is considered when the wind speed at hub height is below or above the rated cut-in or cut-out speeds, respectively. Monthly power downtime averaged over 20 years (2000-2019) is computed for the twelve months of a year, assuming operation of the wind turbine only, and operation of the hybrid platform, with wind and wave power.

Power downtime is plotted as fraction percentage time during each month in the polar plots of Figure 8a, Figure 8b and Figure 8c, for VS, NE3 and NE8, respectively. In the figures, the areas delimited by the monthly downtime are delimited with dotted lines and are lightly shaded for the case of the wind turbine. While, for the hybrid platform case, the downtime areas are delimited with solid lines and darkly shaded. Red, blue and black colours are used for VS, NE3 and NE8, respectively. The polar plots of Figure 8 show that power downtime increases during the summer months and decreases towards the winter months in the three locations. This behaviour is associated to the seasonal availability of the resources shown in Figure 6.

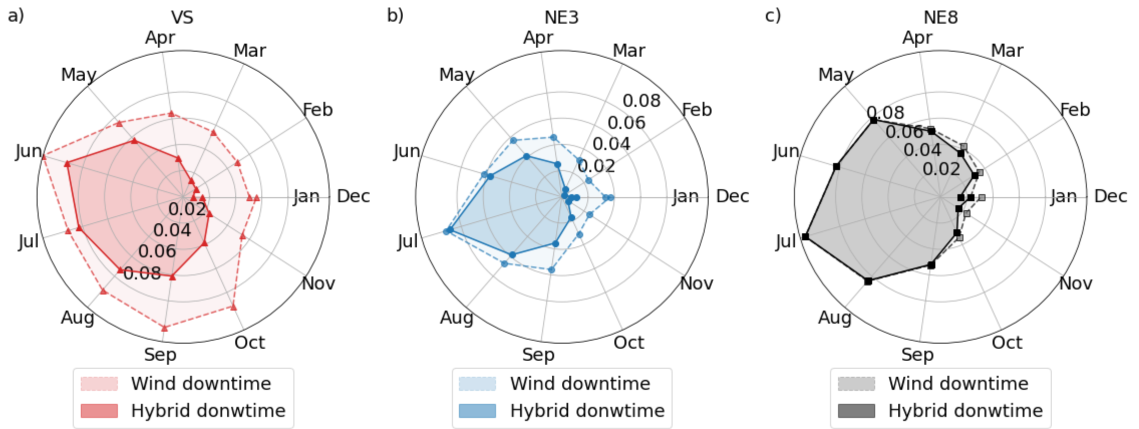

Figure 8: Monthly average wind power downtime limited with dotted lines and lightly shaded colors versus hybrid power downtime limited by solid lines and darkly shaded colors during a 20 year period (2000-2019) for a) VS, b) NE3 and c) NE8.

In terms of wind power downtime, the polar plots show that the wind power downtime is higher in VS (Figure 8a), followed by NE8 (Figure 8c) and then by NE3 (Figure 8b). The yearly downtime average are 7.4%, 5.4% and 4.7% for VS, NE8 and NE3, respectively. To understand these patterns, it is necessary to average the monthly wind power density values shown in Figure 6a. Wind power density values for VS, NE8 and NE3 are 0.81×10^3 W/m^2, 1.01×10^3 W/m^2 and 1.08×10^3 W/m^2, respectively. Hence, the higher the wind power density of a site, the lower the associated wind power downtime, and vice versa.

In terms of hybrid power performance, the polar plots show that power downtime reduction is the highest in VS (Figure 8a), followed by NE3 (Figure 8B), and very minimal for NE8 (Figure 8c). Specifically, the highest power downtime reduction between wind turbine and hybrid platform case occurs in VS, with an average yearly reduction from 7.4% downtime to 4.2% downtime. For NE3, the yearly power downtime reduction goes from 4.7% to 3.0%. Lastly, for NE8, the drop in power downtime goes from 5.4% to 5.1%.

The power downtime performance of the hybrid platform is dependent on the performance of the wave energy converter and on the selection of wave power threshold. However, wave power density and wind and wave correlation indices are determining factors as well. By averaging the monthly wave power density values shown in Figure 6b, we obtain $\rho_{wave} = 3.96 \times 10^5$ W/m, $\rho_{wave} = 4.24 \times 10^5$ W/m and $\rho_{wave} = 1.67 \times 10^5$ W/m for VS, NE3 and NE8, respectively. While the yearly averaged wind and wave correlation indices are 0.35, 0.63 and 0.78 for VS, NE3 and NE8, respectively. Hence, the location with one of the highest yearly ρ_{wave} and with the lowest yearly correlation index, VS, shows the highest average percentage drop in power downtime with a drop of 43% when the hybrid platform is in operation. In second place, NE3 , with the highest yearly ρ_{wave} and intermediate correlation index, shows an intermediate drop in performance with a drop of 36%. In last place, NE8, shows a drop of only 6%, because of the lowest ρ_{wave} and highest correlation index.

These results suggest that the hybrid platform is more effective in reducing power downtime in locations with high wave power density and with low or intermediate wind and wave correlation indices, such as VS and NE3, which are swell dominated regions facing the European Atlantic Coast, as depicted in Figure 2.

Sensitivity analysis

The previous sections considered 1 MW, as the criterion to determine whether wave power was available in the hybrid platform, and therefore, whether wind power downtime reduction occurred. Nonetheless, because the selection of the wave power threshold can change, it is important to evaluate the performance of the hybrid platform subject to different thresholds. Hence, in Figure 9, we compute the power downtime in the three locations, VS, NE3 and NE8 subject to different wave power thresholds. The horizontal axis of Figure 9 shows the wave power threshold ranging from 0.1 MW to 10 MW. We recall that when wave power is equal or above the threshold, power production is considered available. Therefore, the hybrid wind and wave power downtimes, subject to different wave power threshold, are plotted for VS, NE3 and NE8, with different markers as specified in the legend of Figure 9. In Figure 9, dotted lines are used to interpolate the markers. For comparison, Figure 9 also shows the power downtime due to wind only for the three locations, VS, NE3 and NE8, as flat horizontal lines, showing 7.4%, 4.7% and 5.4% downtime, respectively.

Figure 9 shows that reduction in power downtime is still feasible up to 2 MW in VS and NE3. For example, considering a 1 MW threshold, we recall that power downtime drops by approximately 43% in VS and 36% in NE3. Considering a 2 MW threshold, these numbers change to 19% and 17%, respectively. Furthermore, the blue dotted line in Figure 9 reveals that over the range of 0.3 MW to 2 MW wave power threshold, a steep drop in power is achieved in VS. In contrast, the black dotted line shows that for NE3, a more gradual and uniform drop in power is obtained over the same wave power threshold range. The red dotted line shows that for NE8, a gradual and less steep drop in power occurs, extending from 100 kW to approximately 1 MW.

As the wave power threshold increases to 3 MW in VS and NE3, and to 1 MW in NE8, the hybrid power downtime curves asymptote to similar downtime levels where only wind power is considered, i.e. the baseline cases. Therefore, the sensitivity analysis shown in Figure 9 highlights that the performance of the hybrid platform is superior in high wave power density locations with low to intermediate correlation. However, the hybrid platform can also perform satisfactorily in low wave power density and high correlation locations, provided that the wave power threshold is relaxed to lower thresholds. In the case of Figure 9, to thresholds below 1 MW.

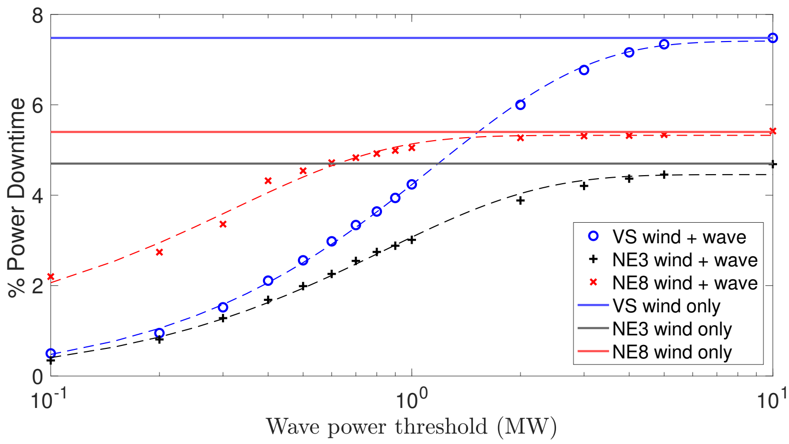

Figure 9: Different wave power thresholds versus average percentage power downtime computed with metocean data during 20 years (2000-2019) for VS, NE3 and NE8.Scattered points show the hybrid power downtime, with the scattered markers interpolated with dotted lines. Solid lines denote power downtime for the wind turbine only.

6 Discussion

The results obtained in this work highlight that a hybrid wind wave platform is functional for applications where a minimum power baseload is required. For example, the case of PEM electrolysers, which are designed to operate in steady state, and cycles of on and off switching are preventable if at least 20% of their power rating is provided. Considering the case of the hybrid platform and a 5 MW wind turbine, then a minimum baseload of 1 MW would be required to keep a 5 MW electrolyser continuously running (27).

The sensitivity analysis carried out in the previous section showed that the hybrid platform can reduce effectively the power downtime over a range of wave power thresholds and up to 2 MW in high wave energy density and low wind and wave correlation locations. However, it is important to mention that the wave energy conversion system of the hybrid platform can be improved through hull geometry or parallel arrays of platforms. As such, the disparity between wave and wind power can be reduced. Furthermore, the smoothness of the power output can be increased, by reducing the scale of the wind turbine. Hence, the design of the hybrid platform can be modified according to different performance objectives.

An important consideration for performance of wind wave hybrid platforms is the metocean properties of the selected site. High wave power density with low correlation sites are locations where the hybrid platform shows the highest drop in wind downtime power. This is because wave power is more available due to the high energy contained in swell waves. Additionally, the complementary of wind and wave resources is highest in low correlation sites. In contrast, although the hybrid platform can also provide power downtime reduction in high correlation sites, the fact that wave power density is typically lower due to enclosed basins surrounded by land masses, signifies a slight reduction in performance of the hybrid platform. Hence, ideally, hybrid wind wave platforms are suitable for open sea swell dominated locations, where wind and wave resource have low to intermediate correlation indices (C $\leq$ 0.7).

Lastly, note that the selection of wave power as the principal complement of wind energy over other sources of renewable energy, such as solar energy, is preferred due to a reduced footprint in surface area requirements. This is important because firstly, a lower surface area footprint reduces manufacturing costs, and secondly, it allows scalability with platforms in parallel.

7 Conclusions

This paper develops the concept of a hybrid wind and wave floating platform to provide a minimum power base load for offshore applications. We consider the case of PEM electrolysers in an independent floating station, whose operational life is reduced when the power baseload drops below 20% of their rated capacity (27). For a system that includes a 5 MW wind turbine supplying power to a 5 MW PEM elctrolyser, the minimum required baseload is 1 MW. Hence, in this work, we design a hybrid wind wave platform to supply that minimum baseload. Consequently, wave power reduces the downtime in which the PEM electrolyser would have to be shut down in only wind power was available.

In order to assess the performance of the hybrid platform to reduce wind power downtime and to supply a minimum power baseload, three different locations are considered: One off the coast of Spain (VS), and two off the coast of Scotland, one on the west coast (NE3) and one in the North Sea (NE8). The sites were selected to evaluate the hybrid platform subject to low, intermediate and high wind wave correlation indices, respectively. The hybrid platform is composed of three pontoons interconnected by two hinges. A numerical model to compute wave power was developed for the hybrid platform, which converts hinge motion to wave energy. A 5 MW wind turbine is mounted on deck and downstream of the platform. Due to reduced pitch motions downstream of the floating platform and control capabilities of the wind turbine, the power curve of the 5 MW wind turbine is considered. Therefore, based on the design considerations above, the main findings of the manuscript are summarised as follows:

1. The influence of a 5MW wind turbine in the motion of the platform was assessed. Assuming average wind turbine loading, it was observed that the turbine is not detrimental to hinge motion performance, and therefore hinge motion of the hybrid platform can be deployed for wave energy extraction.
2. The platform is free to yaw through a single point mooring line upstream of the platform. Hence, the wind turbine is installed downstream of the platform, where motion is minimised by the upstream hinge. The upstream hinge, acts as a motion suppressor to the downstream hinge. Importantly, as demonstrated in the literature, as long as the pitching motion of the turbine is reduced, then, the mean wind power production remains unaffected (45).
3. In this work, two mechanisms reduce the pitching motions of the downstream hinge. One is the passive reduction of pitching motions through more energy absorption of the upstream hinge. The second one is active, through setting the PTO damping to operate in optimum power conditions.
4. A power matrix for the hybrid platform was developed, considering irregular waves, through the superposition of discrete waves from a JONSAWP wave spectrum. Wave power production of the platform is broadband due to the presence of the two hinges, and is highest between $10\,s \leq T_s \leq 14\,s$, which is a region of significant wave power in multiple world locations (5; 4). Naturally, wave power increases also with wave height.
5. Metocean data analysis of 20 years revealed that wind power downtime is inversely proportional to wind power density, and that the ability of the platform to provide a minimum power base load relies on two main factors: Firstly, high wave power density. Secondly, low to intermediate wind and wave correlation index. Hence, swell dominated regions with low wind and wave correlation indices are ideal for this type of hybrid platform.

6. Assuming that $\mathrm{downtime} = \mathrm{wave\,power} < 1\,\mathrm{MW}$, analysis of 20 years of metocean data at the three selected locations (VS, NE3 and NE8) reveal that the hybrid platform decreases wind power downtime in VS and NE3 by 43% and 36%, respectively, with respect to the total time of wind power downtime. This is equivalent to a reduction of 5,500 and 3,000 downtime hours, in VS and NE3, respectively.
7. Sensitivity analysis shows that power thresholds of up to 2 MW can provide a significant reduction in wind power downtime in VS and NE3. In NE8, power downtime could be achieved by lowering the wave power threshold to the kW range.

In summary, the hybrid wind and wave platform presented in this work is able to provide a minimum power threshold for offshore applications that suffer from periods of time where wind power is absent, and that require a minimum level of power for continuous operation. The design of the hybrid platform is scalable, and can be tailored to other applications in which smoothness of power is also relevant, making the current design a versatile concept that can prolong the life of different offshore applications and also, provide an alternative route to tackle wind intermittency and energy storage, through hybrid wind wave power generation.

8 Acknowledgments

This work was funded by the UK Engineering and Physical Sciences Research Council (EPSRC) as part of the Ocean-REFuel (Ocean Renewable Energy Fuels) Programme Grant EP/W005212/1 awarded to the University of Strathclyde, Newcastle University, University of Nottingham, Cardiff University and Imperial College London. This work also received funding as part of the Supergen ORE Impact Hub 2023 Programme Grant EP/Y016297/1 and an Early Career Research Grant from the Supergen ORE Impact Hub 2023. The first author would like acknowledge Yongqiang Chen from Shanghai Jiao Tong University for providing the hydrodynamic coefficients utilised to compute the dynamic response of the hinged VLFS.

A Appendix 1 - Moments of inertia

In Equation 4, the mass matrix **M** is defined as

$$\mathbf{M_j} = \begin{bmatrix} \mathbf{M}_1 & & & & \\ & \mathbf{M}_2 & & & \\ & & \ddots & & \\ & & & \ddots & \\ & & & & \mathbf{M}_N \end{bmatrix} \tag{13}$$

where j indicates the submodule of each pontoon of the VLFS. The j-th M matrix is composed by

$$\mathbf{M_j} = \begin{bmatrix} m & 0 & 0 & 0 & 0 & 0 \\ 0 & m & 0 & 0 & 0 & 0 \\ 0 & 0 & m & 0 & 0 & 0 \\ 0 & 0 & 0 & I_x & 0 & 0 \\ 0 & 0 & 0 & 0 & I_y & 0 \\ 0 & 0 & 0 & 0 & 0 & I_z \end{bmatrix} \tag{14}$$

where m is the mass of the submodule, I_x, I_y and I_z are the mass moments of inertia with respect to x, y and z. The corresponding masses and moments of inertia for the N-the module that sustains the wind turbine is computed considering the inertia of the rotor-nacelle assembly and of the tower (8), and translating the moments to the base of the turbine through the the parallel axis theorem, as specified in Appendix 1 from this manuscript. The local frame of references for the N-th submodule of the VLFS, the tower and the RNA are depicted in the schematic of Figure 10.

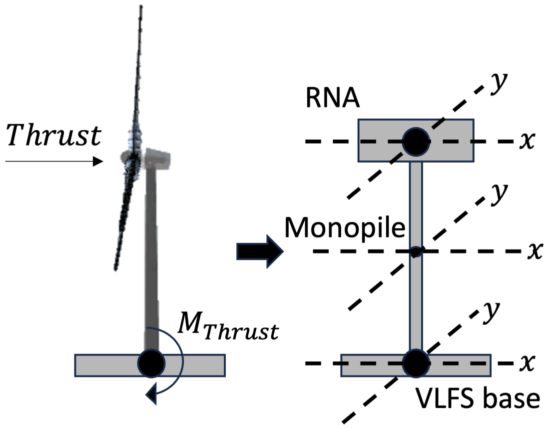

Figure 10: Frames of references for N-th module of the VLFS sustaining the wind turbine, the tower and the RNA.

Lastly, the local mass moments of inertia are translated to the base of the N-the submodule through the parallel axis theorem, such that

VLFS	VLFS + WT
m	$m^{'} = m + m_{mp} + m_{RNA}$
I_{xx}	$I^{'}_{xx} = I_{xx} + I_{xxmp} + m_{mp}r^2_{mp} + I_{xxRNA} + m_{RNA}r^2_{RNA}$
I_{yy}	$I^{'}_{yy} = I_{yy} + I_{yymp} + m_{mp}r^2_{mp} + I_{yyRNA} + m_{RNA}r^2_{RNA}$
I_{zz}	$I^{'}_{zz} = I_{zz} + I_{zzmp} + m_{mp}r^2_{mp} + I_{zzRNA} + m_{RNA}r^2_{RNA}$

References

[1] Allen, C., Viscelli, A., Dagher, H., Goupee, A., Gaertner, E., Abbas, N., Hall, M., and Barter, G. (2020). Definition of the umaine volturnus-s reference platform developed for the iea wind 15-megawatt offshore reference wind turbine. Technical report, National Renewable Energy Lab.(NREL), Golden, CO (United States); Univ. of ....

[2] Arredondo-Galeana, A. and Brennan, F. (2021). Floating offshore vertical axis wind turbines: Opportunities, challenges and way forward. *Energies*, 14(23), ISSN: 1996-1073, DOI: 10.3390/en14238000.

[3] Arredondo-Galeana, A., Dai, S., Chen, Y., Zhang, X., and Brennan, F. (2023a). Understanding the force motion trade off of rigid and hinged floating platforms for marine renewables. *Proceedings of the European Wave and Tidal Energy Conference*, 15, DOI: 10.36688/ewtec-2023-389, https://submissions.ewtec.org/proc-ewtec/article/view/389.

[4] Arredondo-Galeana, A., Ermakov, A., Shi, W., Ringwood, J. V., and Brennan, F. (2024). Optimal control of wave cycloidal rotors with passively morphing foils: An analytical and numerical study. *Marine Structures*, 95:103597, ISSN: 0951-8339, DOI: https://doi.org/10.1016/j.marstruc.2024.103597, https://www.sciencedirect.com/science/article/pii/S095183392400025X.

[5] Arredondo-Galeana, A., Olbert, G., Shi, W., and Brennan, F. (2023b). Near wake hydrodynamics and structural design of a single foil cycloidal rotor in regular waves. *Renewable Energy*, 206:1020–1035, ISSN: 0960-1481, DOI: https://doi.org/10.1016/j.renene.2023.02.068, https://www.sciencedirect.com/science/article/pii/S0960148123002124.

[6] Astariz, S. and Iglesias, G. (2017). The collocation feasibility index – a method for selecting sites for co-located wave and wind farms. *Renewable Energy*, 103:811–824, ISSN: 0960-1481, DOI: https://doi.org/10.1016/j.renene.2016.11.014, https://www.sciencedirect.com/science/article/pii/S0960148116309776.

[7] Bastos, P., Devoy-McAuliffe, F., Arredondo-Galeana, A., Chozas, J. F., Lamont-Kane, P., and Vinagre, P. A.

(2023). Life cycle assessment of a lift-based wave energy converter. In *Proceedings of the European Wave and Tidal Energy Conference*, volume 15, pages 1–10.

[8] Bir, G. and Jonkman, J. (2008). Modal dynamics of large wind turbines with different support structures. In *International conference on offshore mechanics and arctic engineering*, volume 48234, pages 669–679.

[9] Borg, M., Collu, M., and Brennan, F. P. (2013). Use of a wave energy converter as a motion suppression device for floating wind turbines. *Energy Procedia*, 35:223–233, ISSN: 1876-6102, DOI: https://doi.org/10.1016/j.egypro.2013.07.175, https://www.sciencedirect.com/science/article/pii/S1876610213012617. DeepWind'2013 – Selected papers from 10th Deep Sea Offshore Wind R&D Conference, Trondheim, Norway, 24 – 25 January 2013.

[Bureau Veritas] Bureau Veritas. Hydrostar software: A powerful hydrodynamic tool. https://marine-offshore.bureauveritas.com/hydrostar-software-powerful-hydrodynamic. Accessed: 17-Mar-2025.

[11] Chen, D., Feng, X., Li, Z., and Chen, J.-F. (2023). Long-term extreme responses of torsional moments at two-directional hinges for moored very large floating structures. *Ocean Engineering*, 290:116330, ISSN: 0029-8018, DOI: https://doi.org/10.1016/j.oceaneng.2023.116330.

[12] Chowdhury, M. S., Rahman, K. S., Selvanathan, V., Nuthammachot, N., Suklueng, M., Mostafaeipour, A., Habib, A., Akhtaruzzaman, M., Amin, N., and Techato, K. (2021). Current trends and prospects of tidal energy technology. *Environment, Development and Sustainability*, 23(6):8179–8194, ISSN: 1573-2975, DOI: 10.1007/s10668-020-01013-4, https://doi.org/10.1007/s10668-020-01013-4.

[13] DNV (2007). *Recommended Practice DNV-RP-C205. Environmental conditions and environmental loads*. Det Norske Veritas, Høvik, Norway.

[14] Folley, M. and Whittaker, T. (2010). Spectral modelling of wave energy converters. *Coastal Engineering*, 57(10):892–897, ISSN: 0378-3839, DOI: https://doi.org/10.1016/j.coastaleng.2010.05.007, https://www.sciencedirect.com/science/article/pii/S0378383910000700.

[15] Gao, Q., Khan, S. S., Sergiienko, N., Ertugrul, N., Hemer, M., Negnevitsky, M., and Ding, B. (2022). Assessment of wind and wave power characteristic and potential for hybrid exploration in australia. *Renewable and Sustainable Energy Reviews*, 168:112747, ISSN: 1364-0321, DOI: https://doi.org/10.1016/j.rser.2022.112747, https://www.sciencedirect.com/science/article/pii/S1364032122006347.

[16] Ghafari, H. R., Ghassemi, H., and He, G. (2021). Numerical study of the wavestar wave energy converter with multi-point-absorber around deepcwind semisubmersible floating platform. *Ocean Engineering*, 232:109177, ISSN: 0029-8018, DOI: https://doi.org/10.1016/j.oceaneng.2021.109177, https://www.sciencedirect.com/science/article/pii/S0029801821006107.

[17] Gubesch, E., Sergiienko, N. Y., Nader, J.-R., Ding, B., Cazzolato, B., Penesis, I., and Li, Y. (2023). Experimental investigation of a co-located wind and wave energy system in regular waves. *Renewable Energy*, 219:119520, ISSN: 0960-1481, DOI: https://doi.org/10.1016/j.renene.2023.119520, https://www.sciencedirect.com/science/article/pii/S0960148123014350.

[18] Guo, B. and Ringwood, J. V. (2021). A review of wave energy technology from a research and commercial perspective. *IET Renewable Power Generation*, 15(14):3065–3090, DOI: https://doi.org/10.1049/rpg2.12302, https://ietresearch.onlinelibrary.wiley.com/doi/abs/10.1049/rpg2.12302.

[19] Ioannou, A., Liang, Y., Jalón, M., and Brennan, F. (2020). A preliminary parametric techno-economic study of offshore wind floater concepts. *Ocean Engineering*, 197:106937, ISSN: 0029-8018, DOI: https://doi.org/10.1016/j.oceaneng.2020.106937, https://www.sciencedirect.com/science/article/pii/S0029801820300214.

[20] Jin, S. and Greaves, D. (2021). Wave energy in the uk: Status review and future perspectives. *Renewable and Sustainable Energy Reviews*, 143:110932, ISSN: 1364-0321, DOI: https://doi.org/10.1016/j.rser.2021.110932, https://www.sciencedirect.com/science/article/pii/S1364032121002240.

[21] Jonkman, J., Butterfield, S., Musial, W., and Scott, G. (2009). Definition of a 5-mw reference wind turbine for offshore system development. Technical report, National Renewable Energy Lab.(NREL), Golden, CO (United States).

[22] Jonkman, J. M. and Buhl Jr., M. L. (2007). Loads analysis of a floating offshore wind turbine using fully coupled simulation: Preprint. United States. https://www.osti.gov/biblio/909454. Research Org.: National Renewable Energy Lab. (NREL), Golden, CO (United States).

[23] Kalogeri, C., Galanis, G., Spyrou, C., Diamantis, D., Baladima, F., Koukoula, M., and Kallos, G. (2017). Assessing the european offshore wind and wave energy resource for combined exploitation. *Renewable Energy*, 101:244–264, ISSN: 0960-1481, DOI: https://doi.org/10.1016/j.renene.2016.08.010, https://www.sciencedirect.com/science/article/pii/S096014811630711X.

[LAUTEX ESOX.] LAUTEX ESOX. Available at: https://esox.lautec.com/map/. Accessed: 2023-10-25.

[25] McNatt, J. C. and Retzler, C. H. (2020). The performance of the mocean m100 wave energy converter described through numerical and physical modelling. *International Marine Energy Journal*, 3(1):11–19, DOI: 10.36688/imej.3.11-19, https://marineenergyjournal.org/imej/article/view/44.

[26] Mei, C. C. and Newman, J. N. (1980). Wave power extraction by floating bodies. In *1st Symposium on Wave Energy Utilisation*.

[27] Niblett, D., Delpisheh, M., Ramakrishnan, S., and Mamlouk, M. (2024). Review of next generation hydrogen production from offshore wind using water electrolysis. *Journal of Power Sources*, 592:233904, ISSN: 0378-7753, DOI: https://doi.org/10.1016/j.jpowsour.2023.233904, https://www.sciencedirect.com/science/article/pii/S0378775323012806.

[28] Noad, I. and Porter, R. (2017a). Modelling an articulated raft wave energy converter. *Renewable Energy*, 114:1146–1159, ISSN: 0960-1481, DOI: https://doi.org/10.1016/j.renene.2017.07.077, https://www.sciencedirect.com/science/article/pii/S096014811730705X.

[29] Noad, I. F. and Porter, R. (2017b). Approximations to wave energy absorption by articulated rafts. *SIAM Journal on Applied Mathematics*, 77(6):2199–2223, DOI: 10.1137/16M1104743, https://doi.org/10.1137/16M1104743.

[30] Papi, F. and Bianchini, A. (2022). Technical challenges in floating offshore wind turbine upscaling: A critical analysis based on the nrel 5 mw and iea 15 mw reference turbines. *Renewable and Sustainable Energy Reviews*, 162:112489, ISSN: 1364-0321, DOI: https://doi.org/10.1016/j.rser.2022.112489, https://www.sciencedirect.com/science/article/pii/S1364032122003938.

[31] Pennock, S., Noble, D. R., Vardanyan, Y., Delahaye, T., and Jeffrey, H. (2023). A modelling framework to quantify the power system benefits from ocean energy deployments. *Applied Energy*, 347:121413, ISSN: 0306-2619, DOI: https://doi.org/10.1016/j.apenergy.2023.121413, https://www.sciencedirect.com/science/article/pii/S0306261923007778.

[32] Reikard, G., Robertson, B., and Bidlot, J.-R. (2015). Combining wave energy with wind and solar: Short-term forecasting. *Renewable Energy*, 81:442–456, ISSN: 0960-1481, DOI: https://doi.org/10.1016/j.renene.2015.03.032, https://www.sciencedirect.com/science/article/pii/S0960148115002141.

[33] Rodríguez Castillo, C. A., Collu, M., and Brennan, F. (2025). Comparative design space exploration of centred and off-centred semisubmersible configurations for floating offshore wind turbines. *Ocean Engineering*, 324:120740, ISSN: 0029-8018, DOI: https://doi.org/10.1016/j.oceaneng.2025.120740, https://www.sciencedirect.com/science/article/pii/S002980182500455X.

[34] Rusu, L. and Onea, F. (2017). The performance of some state-of-the-art wave energy converters in locations with the worldwide highest wave power. *Renewable and Sustainable Energy Reviews*, 75:1348–1362, ISSN: 1364-0321, DOI: https://doi.org/10.1016/j.rser.2016.11.123, https://www.sciencedirect.com/science/article/pii/S1364032116308838.

[35] Scarlett, G. T., McNatt, J. C., Henry, A., and Arredondo-Galeana, A. (2024). Energy flux method for wave energy converters. *Energies*, 17(19), ISSN: 1996-1073, DOI: 10.3390/en17194991, https://www.mdpi.com/1996-1073/17/19/4991.

[36] Scarlett, G. T., McNatt, J. C., Henry, A. J., and Arredondo-Galeana, A. (2016). Energy flux method for wave energy converters. *Energies*, 3(3), ISSN: 2226-4310, DOI: 10.3390/energies3030027, https://www.mdpi.com/2226-4310/3/3/27.

[37] Stansby, P. and Li, G. (2024a). Compact hybrid omni-directional wind-wave-solar platforms for range of capacities. In *Innovations in Renewable Energies Offshore*, pages 845–852. CRC Press.

[38] Stansby, P. and Li, G. (2024b). A wind semi-sub platform with hinged floats for omni-directional swell wave energy conversion. *Journal of Ocean Engineering and Marine Energy*, 10(2):433–448, ISSN: 2198-6452, DOI: 10.1007/s40722-024-00321-5, https://doi.org/10.1007/s40722-024-00321-5.

[39] Tay, Z. Y. (2019). Energy extraction from an articulated plate anti-motion device of a very large floating structure under irregular waves. *Renewable Energy*, 130:206–222, ISSN: 0960-1481, DOI: https://doi.org/10.1016/j.renene.2018.06.044, https://www.sciencedirect.com/science/article/pii/S096014811830689X.

[40] Taylor, J. R. (1997). *Introduction to Error Analysis: The Study of Uncertainties in Physical Measurements*. University Science Books, Sausalito, CA, 2nd edition.

[41] Thomassen, P. E., Bruheim, P. I., Suja, L., and Frøyd, L. (2012). A novel tool for fem analysis of offshore wind turbines with innovative visualization techniques. volume All Days of *International Ocean and Polar Engineering Conference*, pages ISOPE–I–12–080.

[42] Tran, T.-T. and Kim, D.-H. (2015). The platform pitching motion of floating offshore wind turbine: A preliminary unsteady aerodynamic analysis. *Journal of Wind Engineering and Industrial Aerodynamics*, 142:65–81, ISSN: 0167-6105, DOI: https://doi.org/10.1016/j.jweia.2015.03.009, https://www.sciencedirect.com/science/article/pii/S0167610515000690.

[43] Veers, P., Dykes, K., Lantz, E., Barth, S., Bottasso, C. L., Carlson, O., Clifton, A., Green, J., Green, P., Holttinen, H., Laird, D., Lehtomäki, V., Lundquist, J. K., Manwell, J., Marquis, M., Meneveau, C., Moriarty, P., Munduate, X., Muskulus, M., Naughton, J., Pao, L., Paquette, J., Peinke, J., Robertson, A., Rodrigo, J. S., Sempreviva, A. M., Smith, J. C., Tuohy, A., and Wiser, R. (2019). Grand challenges in the science of wind energy. *Science*, 366(6464):eaau2027, DOI: 10.1126/science.aau2027, https://www.science.org/doi/abs/10.1126/science.aau2027.

[44] Wang, M., Xingxian bao, Qu, M., Wang, T., and Iglesias, G. (2025). Power performance and motion characteristics of a floating hybrid wind-wave energy system. *Ocean Engineering*, 318:120184, ISSN: 0029-8018, DOI: https://doi.org/10.1016/j.oceaneng.2024.120184, https://www.sciencedirect.com/science/article/pii/S0029801824035224.

[45] Wen, B., Dong, X., Tian, X., Peng, Z., Zhang, W., and Wei, K. (2018). The power performance of an offshore floating wind turbine in platform pitching motion. *Energy*, 154:508–521, ISSN: 0360-5442, DOI: https://doi.org/10.1016/j.energy.2018.04.140, https://www.sciencedirect.com/science/article/pii/S0360544218307564.

[46] Zhang, D., Du, J., Yuan, Z., Yu, S., and Li, H. (2023a). Motion characteristics of large arrays of modularized floating bodies with hinge connections. *Physics of Fluids*, 35(7):077107, ISSN: 1070-6631, DOI: 10.1063/5.0153317, https://doi.org/10.1063/5.0153317.

[47] Zhang, J., Zhao, X., Greaves, D., and Jin, S. (2023b). Modeling of a hinged-raft wave energy converter via deep operator learning and wave tank experiments. *Applied Energy*, 341:121072, ISSN: 0306-2619, DOI: https://doi.org/10.1016/j.apenergy.2023.121072, https://www.sciencedirect.com/science/article/pii/S0306261923004361.

[48] Zhang, X., Lu, D., Guo, F., Gao, Y., and Sun, Y. (2018). The maximum wave energy conversion by two interconnected floaters: Effects of structural flexibility. *Applied Ocean Research*, 71:34–47, ISSN: 0141-1187, DOI: https://doi.org/10.1016/j.apor.2017.12.003, https://www.sciencedirect.com/science/article/pii/S0141118717304789.

[49] Zhang, X., Lu, D., Liang, Y., and Brennan, F. (2021). Feasibility of very large floating structure as offshore wind foundation: Effects of hinge numbers on wave loads and induced responses. *Journal of Waterway, Port, Coastal, and Ocean Engineering*, 147(3):04021002, DOI: 10.1061/(ASCE)WW.1943-5460.0000626.